The impact of nanostructure on hygroscopicity and reactivity of fatty acid atmospheric aerosol proxies

Adam Milsom,[1] Adam M. Squires,[2] Ben Laurence,[2] Ben Woden,[3] Andrew J. Smith,[4] Andrew D. Ward[5] and Christian Pfrang.[1,6,*]

[1]School of Geography, Earth and Environmental Sciences, University of Birmingham, Edgbaston, B15 2TT, Birmingham, UK.

[2]Department of Chemistry, University of Bath, South Building, Soldier Down Ln, Claverton Down, BA2 7AX, Bath, UK.

[3]Department of Chemistry, University of Reading, RG6 6AD, Reading, Berkshire, UK

[4]Diamond Light Source, Diamond House, Harwell Science and Innovation Campus, OX11 0DE, Didcot, UK.

[5]Central Laser Facility, STFC Rutherford Appleton Laboratory, Didcot OX11 0FA, UK

[6]Department of Meteorology, University of Reading, Whiteknights, Earley Gate, RG6 6BB, Reading, UK.

*Corresponding author: Professor Christian Pfrang (c.pfrang@bham.ac.uk)

Abstract

Atmospheric aerosol hygroscopicity and reactivity play key roles in determining an aerosol's fate and are strongly affected by its composition and physical properties. Fatty acids are surfactants commonly found in organic aerosol emissions. They form a wide range of different nanostructures dependent on water content and mixture composition. In this study we follow nano-structural changes in mixtures frequently found in urban organic aerosol emissions, i.e. oleic acid, sodium oleate and fructose, during humidity change and exposure to the atmospheric oxidant ozone. Addition of fructose altered the nanostructure by inducing molecular arrangements with increased surfactant-water interface curvature. Small-Angle X-ray Scattering (SAXS) was employed for the first time to derive the hygroscopicity of each nanostructure by measuring time- and humidity-resolved changes in nano-structural parameters. We found that hygroscopicity is directly linked to the specific nanostructure and is dependent on the nanostructure geometry. Reaction with ozone revealed a clear nanostructure-reactivity trend, with notable differences between the individual nanostructures investigated. Simultaneous Raman microscopy complementing the SAXS studies revealed the persistence of oleic acid even after extensive oxidation. Our findings demonstrate that self-assembly of fatty acid nanostructures can significantly impact two key atmospheric aerosol processes: water uptake and chemical reactivity, thus directly affecting the atmospheric lifetime of these materials. This could have significant impacts on both urban air quality (e.g. protecting harmful urban emissions from atmospheric degradation and therefore enabling their long-range transport), and climate (e.g. affecting cloud formation), with implications for human health and wellbeing.

Introduction

Atmospheric aerosols represent a large uncertainty when considering their impact on the climate (Boucher et al., 2013; Shrivastava et al., 2017) and urban particulate matter makes a

significant contribution to air pollution, affecting air quality and health (Shrivastava et al., 2017; Harrison, 2020; Chan and Yao, 2008; Pöschl, 2005). Organic matter can account for a large portion of aerosol emissions depending on the emission source (Jimenez et al., 2009) and environmental conditions have been shown to affect aerosol composition (Li et al., 2021). There are both anthropogenic and biogenic sources of organic aerosols. Activities such as cooking emit a range of organic compounds which can go on to form secondary organic aerosol (SOA) (Zeng et al., 2020). Cooking emissions have been estimated to add *ca.* 10 % to UK $PM_{2.5}$ emissions (Ots et al., 2016) and have been linked with poor air quality (Stavroulas et al., 2023).

Oleic acid is a fatty acid and a common organic compound found in both cooking (Zeng et al., 2020; Alves et al., 2020; Vincente et al., 2018) and marine emissions (Fu et al., 2013). It is reactive towards common atmospheric oxidants such as ozone and NO_3, making it a model compound for laboratory studies into aerosol properties (Zahardis and Petrucci, 2007; Gallimore et al., 2017; Pfrang et al., 2017; Pfrang et al., 2011; Pfrang et al., 2010; King et al., 2010; Sebastiani et al., 2022; Shiraiwa et al., 2012; Shiraiwa et al., 2010). Other common organic emissions are saccharides (sugars), which are also found in urban (Wang et al., 2006) and biogenic emissions (Fu et al., 2013; Fu et al., 2008; Kirpes et al., 2019). Sugar emissions such as levoglucosan and glucose have been shown to react readily with Criegee intermediates, which are formed during ozonolysis (Enami et al., 2017). The fact that these two common classes of organic compounds (fatty acids and sugars) are found in the same aerosol samples raises the possibility that they are able to interact; for example by a sugar reacting with oleic acid ozonolysis Criegee intermediates, potentially altering the product distribution and adding to the complexity of this reaction mechanism – a possibility explored in this study.

Aerosol phase state has been predicted to vary significantly in the atmosphere and is linked to factors such as composition, humidity and temperature (Shiraiwa et al., 2017; Schmedding et al., 2020). One key influence on aerosol multiphase processes is particle viscosity (Reid et al., 2018) and viscous phases have been identified by field measurements of SOA (Virtanen et al., 2010). Particle viscosity can vary by orders of magnitude between phase states, which means the diffusion coefficients of small molecules through the particle phase also vary and heterogeneous processes (*i.e.* oxidation and water uptake) are affected (Shiraiwa et al., 2011; Koop et al., 2011). Viscous phases can induce diffusion gradients during particle humidification (Alpert et al., 2019; Hosny et al., 2016; Renbaum-Wolff et al., 2013; Zobrist et al., 2011). Particles of oleic acid have also been observed to increase in viscosity as a result of oxidation (Hosny et al., 2016). The fate of organic atmospheric aerosols is therefore strongly influenced by their phase state.

Organic coatings are present on the surface of marine aerosols, where sugars and fatty acids were found to be major constituents (Kirpes et al., 2019). Poor air quality has been linked to high $PM_{2.5}$ surface organic content in Beijing, China (Zhao et al., 2020) and the long-range transport of harmful substances emitted in the urban environment has been attributed to viscous organic coatings and the phase state of the aerosol (Shrivastava et al., 2017; Mu et al., 2018). Analysis of marine aerosols heavily influenced by anthropogenic activity found that fatty acids were present along with Polycyclic Aromatic Hydrocarbons (PAHs) and phthalates, which are known to cause poor health (Kang et al., 2017). There is a long-standing discrepancy between the longer lifetime measured in the field compared to laboratory measurements for oleic acid (Rudich et al., 2007; Wang and Yu, 2021). These observations suggest that aerosols are able to travel far from their sources and that the formation of viscous organic coatings could account for their long-range transport.

Pure oleic acid in the liquid phase exhibits some order by the formation of dimers (Iwahashi et al., 1991). As a surfactant, the addition of its ionic form (sodium oleate) and water can induce the formation of lyotropic liquid crystal (LLC) phases (Tiddy, 1980). These are three-dimensional nanostructures which can vary from spherical and cylindrical micelles to bicontinuous networks and bilayers. The spherical and cylindrical micelles can exist with "normal" (oil in water) or "inverse" (water in oil) curvature; the latter are the class formed by the systems in this paper (Pfrang et al., 2017). In our studies, the spherical inverse micelles can exist as (disordered) "inverse micellar" phases, or as ordered "close-packed inverse micellar" phases, which may have cubic (Fd3m) or hexagonal (P6$_3$/mmc) symmetry. The cylinders typically pack as hexagonal arrays ("inverse hexagonal phase") and the bilayers as "lamellar" stacks. These structures, shown in Figure 1, can be followed by Small-Angle X-ray Scattering (SAXS), which probes the nanometre scale. The close-packed inverse micellar, inverse hexagonal, and lamellar phases all show long-range periodicity, giving rise to Bragg peaks in SAXS patterns whose positions show symmetries and repeat spacings. The (disordered) inverse micellar phase gives a broad hump in SAXS, whose position shifts with micelle size.
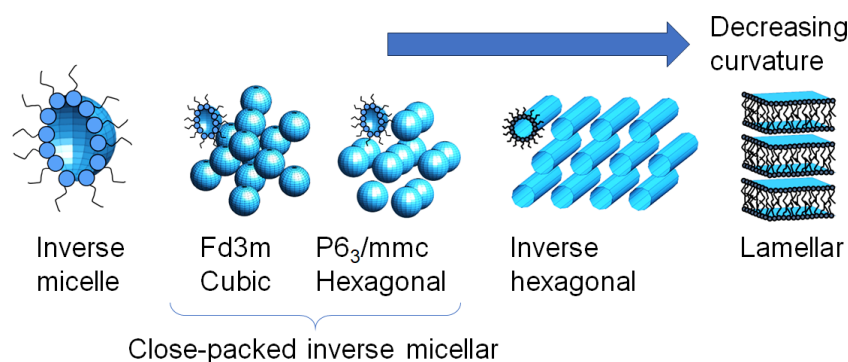
Figure 1: different phases formed by the surfactant systems in this study

Each of these structures exhibit varying physical properties, the key ones being diffusivity and viscosity. Diffusion coefficients can vary dramatically between micellar, close-packed micellar, inverse hexagonal and lamellar phases with diffusion in the latter two becoming directionally dependent (Lindblom and Orädd, 1994; Orädd et al., 1995). The diffusion of atmospherically relevant small molecules, such as ozone and water, would therefore also be affected by the nanostructure formed in the organic medium, affecting the key aerosol heterogeneous processes of water uptake and chemical reaction. While the present study is exploring the behaviour of organic aerosol components, we acknowledge the presence of other components in atmospheric aerosols, specifically inorganic species, which can undergo efflorescence and will add to the complexity of the behaviour of real atmospheric material compared to our organic-material focussed proxies.

We have previously demonstrated the feasibility of LLC formation in levitated particles of a fatty acid aerosol proxy (Pfrang et al., 2017; Milsom et al., 2023; Milsom et al., 2022a) and have exploited the SAXS experiment to quantify the effect of self-assembly on reaction kinetics (Milsom et al., 2021a), along with modelling of the potential impact on the atmospheric lifetime of LLC formation (Milsom et al., 2022b). In this study we coat capillaries with a self-assembled oleic acid/sodium oleate/fructose proxy use SAXS to follow changes in these nanostructures during humidity cycles and exposure to ozone. We investigate the sensitivity of the

126   nanostructure to proxy composition and humidity and demonstrate that reactivity is affected
       by nanostructure.

128

Methods

130   **Preparation of self-assembled coatings inside quartz capillaries**

       The method of film preparation is identical to that described in Milsom et al. (2021a). While
132   coatings inside quartz capillaries will only provide very limited insight on the behaviour of
       coatings on aqueous droplets (which are better approximated by floating self-assembled
134   monolayers at the air-water interface as in previous work, e.g. Pfrang et al., 2014, Woden et
       al., 2018 and Sebastiani et al., 2022), they are good proxies for coatings of solid particles in
136   the atmosphere such as mineral dust. Sample coating solutions were prepared as follows:
       oleic acid (Sigma-Aldrich, 90 %), sodium oleate (Sigma-Aldrich, 99 %) and fructose (Sigma-
138   Aldrich, 99 %) were dissolved as 10 wt % solutions in methanol and samples weighed to the
       desired ratio. All coating solutions are weighed as 1:1:x wt ratio mixtures (oleic acid:sodium
140   oleate:fructose), where x is 0.5, 1, 2 corresponding to 20, 33 and 50 wt % fructose
       compositions.

142   **SAXS experiment and simultaneous Raman microscopy on films coated inside quartz
       capillaries**

144   SAXS probes aggregates at the nanometre scale, measuring order at the molecular, rather
       than atomic (X-ray diffraction), scale (Li et al., 2016; Pauw, 2013). The scattered intensity is
146   measured against a scattering parameter (q) which is proportional to the scattering angle. q is
       inversely proportional to the characteristic spacing between equivalent scattering planes (d)
148   via equation 1. This is also a measure of the spacings between inverse micelles.

$$d = \frac{2\pi}{q} \ (1)$$

150   This d-spacing can be used to determine a range of nano-structural parameters - for example,
       the water layer thickness between lamellar sheets (Kulkarni et al., 2011; Milsom et al., 2022c).

152   This experimental setup is the same as used in our previous capillary film study (Milsom et al.,
       2021a). Key experimental parameters are listed here: SAXS patterns were collected as 1s
154   exposures at different positions along the coated capillary with a delay of 75 s between each
       scan to avoid any X-ray beam damage; the beam size at the sample was approximately 320
156   x 400 µm (FWHM); SAXS patterns were acquired between q = 0.008 – 0.6 Å^{-1} by a *Pilatus
       P3-2M* detector.

158   The Raman microscopy setup is as described in Milsom et al. (2021a): A 532-nm Raman laser
       probe was focussed with a long working distance objective (numerical aperture: 0.42) and a
160   minimum spot diameter of ~ 1.5 µm. The emitted laser power was 20 – 50 mW. By following
       the oleic acid C=C bond peak at ~ 1650 cm^{-1} and normalising to the –CH$_2$ peak at ~ 1442 cm^{-1},
162   we were able to follow the progress of the ozonolysis reaction simultaneous to the SAXS
       measurements.

164   **Controlled humidification of coated films**

       Humidity was monitored and controlled using a bespoke Raspberry Pi (RPi) system. Dry (room
166   air) and wet pumps were controlled by the RPi, in order to reach the target relative humidity
       (RH), which was measured by a sensor at the outlet of the coated capillary tube with a
168   precision of 2 %.

After samples were coated, they were left for ~ 15 min to equilibrate at room humidity (~ 50 –
170 60 % RH) before being attached to the humidity control system. The capillary was then
humidified to the desired settings using the RPi control programme adjusting humidity in the
172 range of ca. 40 to 90% RH.

Ozonolysis of coated films

174 The ozonolysis procedure follows what was set out previously (Milsom et al., 2021a) and is
summarised here: Oxygen (BOC, 99.5 %) was passed through a pen-ray ozoniser (Ultraviolet
176 Products Ltd., Cambridge, UK) which was calibrated offline by UV spectroscopy; the ozone
concentration for all ozonolysis experiments was 77 ± 5 ppm at a flow rate of 60 mL min^{-1}.
178 Note that such a high ozone concentration (atmospheric ozone levels rarely exceed 0.1 ppm)
was used as it is known that self-assembled semi-solid phases slow the rate of reaction
180 significantly (Pfrang et al., 2017; Milsom et al., 2021a). Therefore, comparatively high ozone
concentrations were chosen to be able to observe an oxidative decay during the limited
182 timescale of synchrotron experiments while they are substantially higher than those generally
encountered in the atmosphere. The ozone-oxygen mixture was measured to be at < 5 % RH.

184 Film thickness was determined by X-ray beam attenuation using diodes measuring the
incident and transmitted intensities. The maximum attenuation was determined by filling a
186 capillary with sample material. The thickness of each coated film was then calibrated by
comparison with the filled capillary's attenuation.

188

Results and Discussion

190 **Time- and humidity-resolved nanostructure changes**
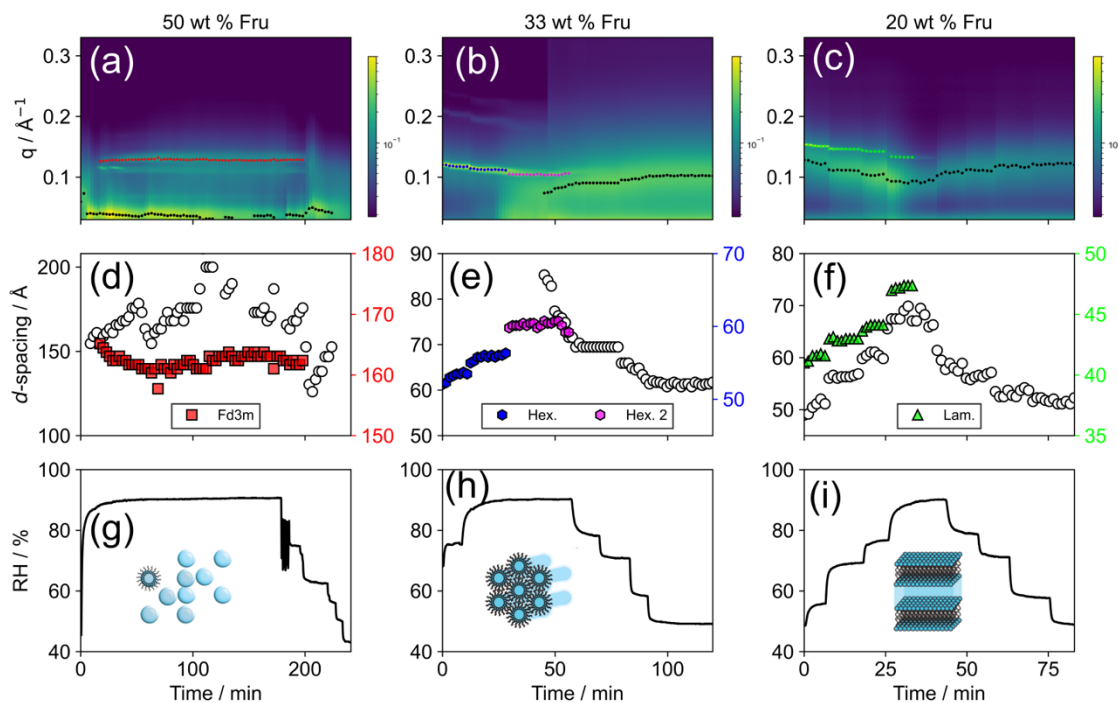
192 Figure 2. (a)-(c) SAXS patterns as a function of time during the humidity cycle. Peak positions
for inverse micellar (black markers) and specific nanostructures (coloured markers) are *q*
194 values corresponding to the time-resolved d-spacings represented in (d)-(f). (g)-(i)
Simultaneous RH vs time during the experiment. Each set of SAXS, *d*-spacing and RH data

196   is presented for each proxy fructose composition as wt % of organic mass with oleic acid and sodium oleate in a 1:1 wt ratio: (a), (d), (g) – 50 wt %; (b), (e), (h) – 33 wt %; (c), (f), (i) – 20 wt

198   % (*i.e.* 50 wt % fructose is a 1:1:2 oleic acid:sodium oleate:fructose mixture). The additional phases co-existing with the (disordered) inverse micellar phase are the cubic close-packed

200   inverse micellar (Fd3m) phase (a,d,g); two different inverse hexagonal phases (b,e,h); and the lamellar phase (c,f,i).

202   Different amounts of fructose in the organic mixture result in different self-assembled nanostructures (Fig. 2(a)-(c)). The inverse micellar phase is seen in all experiments, and this

204   co-exists with cubic close-packed inverse micellar, inverse hexagonal, and lamellar phases at 50 wt% fructose, 33 wt% fructose and 20 wt% fraction, respectively. From first principles

206   fructose, as a hydrophilic water-soluble molecule, would be expected to facilitate water uptake into the organic phase and act as a humectant (moisture attracting agent), analogous to the

208   effect glycerol has on LLC phase boundaries (Richardson et al., 2015). By this logic, larger amounts of fructose should afford more hydrated phases at a given humidity. This can indeed

210   be seen from a comparison of the inverse micellar spacings at high relative humidity (Figures 2 & 3). However, this does not explain the formation of a close-packed inverse micellar phase

212   at 50 wt% fructose vs. inverse hexagonal at 33 wt% fructose, and lamellar at 20 wt% fructose. We suggest that an additional effect is observed during our experiments: the water-surfactant

214   interfacial curvature increases with increasing fructose concentration (Figure 1). This is clear evidence for fructose acting as a *kosmotrope* – a water-structure-inducing molecule (Kulkarni

216   et al., 2011; Libster et al., 2008; Koynova et al., 1997). As a kosmotrope, fructose removes water from the water-surfactant interface. This reduces the effective surfactant headgroup

218   area, enabling the formation of structures with increased curvature at a given water content (in this case, experimental humidity – see corresponding cartoons of each phase in Fig. 1).

220   The phase boundary therefore shifts according to the amount of fructose in the mixture. A set of fructose content-dependent nanostructures are possible as a result. Each one of these

222   nanostructures possesses unique physical properties (as set out in the introduction). The sensitivity of the nanostructure to the amount of fructose in the system suggests that the

224   physical properties, which influence atmospheric trace gas uptake, could also change with similar sensitivity to aerosol composition.

226   The characteristic *d*-spacing for each of the observed nanostructures increases with increasing RH (Fig 2. (d)-(f)). This is the result of water filing the aqueous cavity in the inverse

228   LLC nanostructures observed here. The time and humidity-resolved SAXS patterns acquired in this study have allowed us to take advantage of this characteristic and observe subtle RH-

230   dependent changes in this parameter and directly measure the water uptake of a specific phase. This analysis can be applied to two coexistent phases, provided their SAXS peaks do

232   not overlap – as is the case in our study. The effect of these phases on water uptake is explored in the *Hygroscopicity of observed nanostructures* section.

234   The phase change observed when going from low to high RH is not reversible for the two organic compositions which initially formed inverse hexagonal and lamellar phases at < 90 %

236   RH (Fig. 2(b) and (c)). This suggests that the initial or final phases observed are meta-stable (e.g. the Fd3m and P6$_3$/mmc inverse micellar cubic phases can occur under the same

238   conditions for this system; Pfrang et al., 2017). Fig. 2(d–f) shows that for a given phase equilibrated with water vapour at a particular RH, the *d*-spacing is stable. This suggests that

240   these phases are in equilibrium, even if they are meta-stable.

    For the 33 wt % fructose mixture, a second inverse hexagonal phase appears at high RH

242   before eventually transitioning to an inverse micellar phase (Fig. 2(b) and (e)). Indeed, between ~ 40 – 60 min the inverse micellar and hexagonal phase are observed simultaneously

244   in the mixture. There therefore is a heterogeneity in terms of molecular order and physical properties associated with each of these nanostructures. This coexistent inverse micellar
246   phase is observed for all mixtures studied here.

The 50 wt % fructose mixture exhibits a reversible phase transition from inverse micellar to a
248   cubic close-packed inverse micellar (Fd3m) phase during a humidification-dehumidification cycle (Fig. 2(a)). The Fd3m phase appeared only at the highest humidity setting (90 % RH).
250   The phase transition does not involve a significant change in phase topology, making the transition more facile compared with the transition to an inverse hexagonal or lamellar phase
252   - although the Fd3m arrangement is thought to include inverse micelles of differing size (Seddon et al., 1990; Shearman et al., 2010).

254
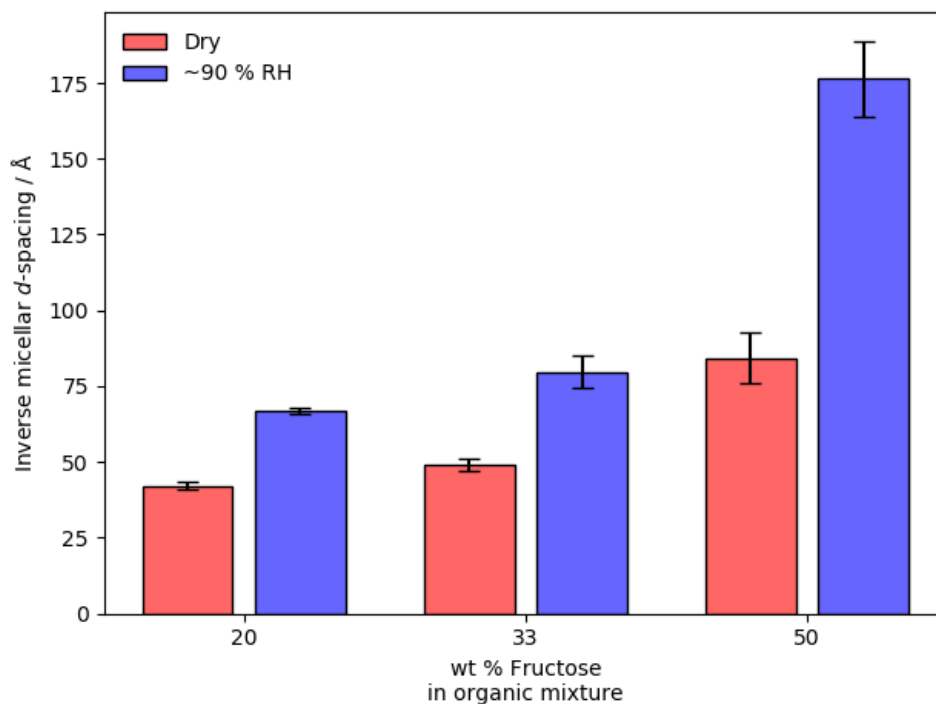
Figure 3. Inverse micellar *d*-spacing vs wt % fructose in the organic mixture under dry (~ 5 %
256   RH) and humid (~ 90 % RH) conditions. A clear increase in *d*-spacing is visible upon humidification of each organic film.

258   A coexistent inverse micellar phase is observed for all organic compositions during these humidity experiments (Fig. 2(a)-(c) – broad peak at lower *q* values). This coexistence
260   represents a heterogeneity within the organic film, implying a similar heterogeneity in physical properties. We cannot say for certain whether this phase separation is uniform throughout the
262   film using this technique. However, the visible shift in the inverse micellar peak position during humidity changes suggests that the change is happening in the majority of the film *i.e.* the
264   inverse micellar is distributed throughout the film.

The inverse micellar *d*-spacing increases with the amount of fructose in the mixture under dry
266   and humid conditions (Fig. 3). The inverse micellar phase observed for all fructose-containing mixtures studied here has a much larger *d*-spacing than mixtures without fructose, where a *d*-
268   spacing of ~28-32 Å is expected (Fig. S1 – SAXS of a hydrated levitated particle of this composition; Mele et al., 2018). Fructose therefore stabilises larger inverse micelles. Notably,
270   under dry (~5 % RH) conditions fructose seems to have a marked effect on the inverse micellar *d*-spacing. This implies that fructose is collecting within the inverse micellar core and that

272 possibly some water has been accommodated within the structure, explaining the increase in the average repeat distance between inverse micelles.

274 Increasing the humidity substantially increases the inverse micellar *d*-spacing for all compositions. This effect is most potent for the 50 wt % fructose mixture (Fig. 3). The

276 observation highlights the ability of fructose to act as a humectant and stabilise large inverse micelles. It is worth restating that these inverse micellar phases at high RH are coexistent with

278 more ordered phases. A measure of the hygroscopicity for each coexistent phase can be extracted from the SAXS data and is presented in the *Hygroscopicity of observed*

280 *nanostructures* section.

282 **Hygroscopicity of observed nanostructures**

We have compared the hygroscopicity of the observed phases with what can be calculated

284 from Raoult's law for fructose over the RH range studied here.
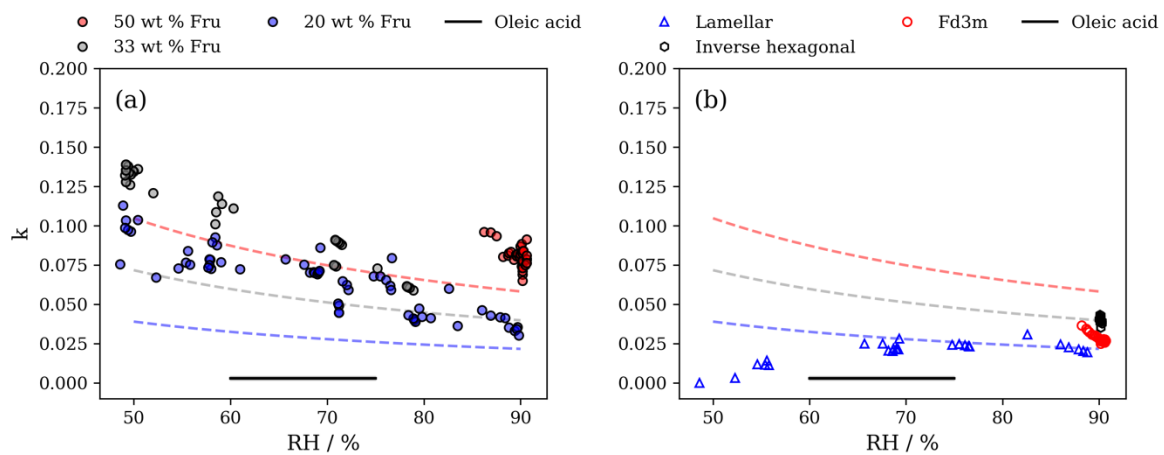
Figure 4. Plots of hygroscopicity parameter (*κ*) derived from *d*-spacings vs RH for the inverse

286 micellar phases at different weight percentage fructose (wt % Fru) (a) and for other nanostructures including the lamellar phase (at 20 wt % fructose), inverse hexagonal (at 33

288 wt % fructose) and close-packed inverse micellar (Fd3m, at 50 wt % fructose) (b). Dashed lines on both plots represent *κ* calculated for the same fructose-lipid ratio based on Raoult's

290 law at a particular RH. The colours of the dashed lines correspond to the wt % fructose in the mixture. The *κ* value for oleic acid measured by Rickards et al. (2013) is also plotted for

292 reference (*κ* = 0.003 ± 0.001).

κ-Köhler theory derives aerosol hygroscopicity from particle sizes at different water activities

294 (a_w; Petters and Kreidenweis, 2007). The characteristic *d*-spacing calculated for each nanostructure observed here is related to its water content. We have applied κ-Köhler theory

296 by measuring the change in *d*-spacing with a_w, to describe the hygroscopicity of each phase. RH was converted to a_w (a_w = RH/100) and it is assumed that the proxy film had equilibrated

298 with the humidity inside the capillary (see the rapid change and equilibration of the *d*-spacing observed when changing RH in Fig. 2). Note that κ-Köhler theory is normally applied to aerosol

300 particles linking particle growth with humidity. Here we are not measuring individual particles, we are measuring nanoscale changes in the structural repeat distances, which are correlated

302 with water content. Equation 2 links the dry (V_d) and water (V_w) volumes with a_w and a hygroscopicity parameter (*κ*; Petters and Kreidenweis, 2007).

304 $$\frac{V_w}{V_d} = \frac{a_w}{(1-a_w)}\kappa \quad (2)$$

The calculation of κ is based on the geometry of each phase and the information regarding
306 the mass and volume fractions of the lipid and water regions derivable from the equilibrium d-
spacings obtained by SAXS (Asghar et al., 2015; Kulkarni et al., 2011). A detailed explanation
308 of the calculation of κ is provided in the ESI.

This parameterisation of hygroscopicity is based on a simplified model which does not account
310 for non-ideal solution behaviour. Also, these experiments are not carried out on particle
ensembles or single particles, as has been the application previously (Liu et al., 2021;
312 Rickards, 2013). As theories of hygroscopicity are in general agreement at higher a_w (RH)
(Rickards, 2013; Clegg et al., 1998; Wexler and Clegg, 2002; Fredenslund et al., 1975;
314 Topping et al., 2005; Zuend et al., 2008; Zuend et al., 2011), our measurements of κ at high
RH (maximum 90 % RH) are the most informative. However, we caution the over-interpretation
316 of these κ values in the context of other hygroscopicity studies due to the experimental
differences between this study and others. These κ measurements do however provide a first
318 insight into the hygroscopic behaviour of these nanostructures and comparison between these
results is justified by the same method used to calculate κ.

320 The hygroscopicity of the disordered inverse micellar phase formed at each composition is
higher than what is predicted by Raoult's law for fructose (Fig. 4(a)). These predictions assume
322 that it is only the fructose that takes up water. Therefore, the formation of the inverse micellar
nanostructure, in addition to the hygroscopicity of the fructose, increases κ beyond what would
324 be expected from the hygroscopicity of fructose alone.

The close-packed inverse micellar phase (Fd3m symmetry) appears to be less hygroscopic
326 than the Raoult prediction by a factor of ~ 2 at 90 % RH (Fig. 4(b)). This is in contrast to the
disordered inverse micelles coexistent with this nanostructure (Fig. 4(a)). The key difference
328 between the two nanostructures is that the close-packed inverse micelles are restricted in
space. The inverse hexagonal and lamellar phases are in better agreement with Raoult's law
330 predictions at > 85 % RH (Fig. 4(b)).

The lamellar phase appears to become much less hygroscopic at low RH. This may be
332 because of an increase in the inter-bilayer attractive forces at lower bilayer separations and/or
more restricted alkyl chains resulting from a more crystalline bilayer (Bahadur et al., 2019). A
334 crystalline form of this lamellar bilayer has been observed in similar systems (Tandon et al.,
2001; Milsom et al., 2021b).

336 As a thermodynamic parameter, κ reflects the energy changes involved in changing the nano-
structural parameters associated with phase hydration and dehydration. For the lamellar
338 phase, work must be done in order to overcome inter- and intra-bilayer repulsion when
increasing and decreasing the volume of water between bilayers (Parsegian et al., 1979). To
340 clarify, if there is attraction between bilayers, then it is easier for the lamellar phase to lose
water (i.e. lower κ at lower humidities where there is less distance and greater attraction
342 between bilayers). In the inverse hexagonal phase, the elastic free energy change associated
with a change in cylindrical radius is related to a bending modulus and the curvature of the
344 cylinder, both of which are associated with the bilayer-forming lipid and are affected by the
addition of other interacting molecules (Chen and Rand, 1997). The close-packed inverse
346 micellar phase is more sterically restricted than the disordered inverse micelles. The
disordered inverse micellar phase has the least frustrated hydrocarbon tails out of the
348 nanostructures presented here (*i.e.* they are not constrained close together, as is the case in
the inverse hexagonal and lamellar phases). Removing water from inverse micelles requires
350 more energy to do because of the increased curvature that results, explaining the increased

κ values for inverse micelles compared with the lamellar, inverse hexagonal and inverse cubic close-packed phases under similar conditions. These nanostructure-specific considerations help explain the difference between experiment and prediction.

All κ values derived from our SAXS data are greater than what has been measured for pure oleic acid (Fig. 4; Rickards et al., 2013). The addition of fructose alone does not account for all of the differences in κ observed between pure oleic acid, predictions based on Raoult's law and the nanostructured fatty acid proxy. There must be an effect of the nanostructure formed and this effect is most pronounced for the disordered inverse micellar phase. While the κ values reported here are substantially (up to nearly 50 times) above those previously measured for oleic acid (Rickards et al. (2013), it should be noted that κ values for highly-CCN-active salts such as sodium chloride are still higher (between 0.5 and 1.4; Petters and Kreidenweis, 2007), so that the inorganic fraction may be considerably more relevant than the nanostructure of the organic fraction for the potential of a particle to act as a CCN when considering internal mixtures of organic and inorganic materials in atmospheric particles.

Reactivity-nanostructure relationship
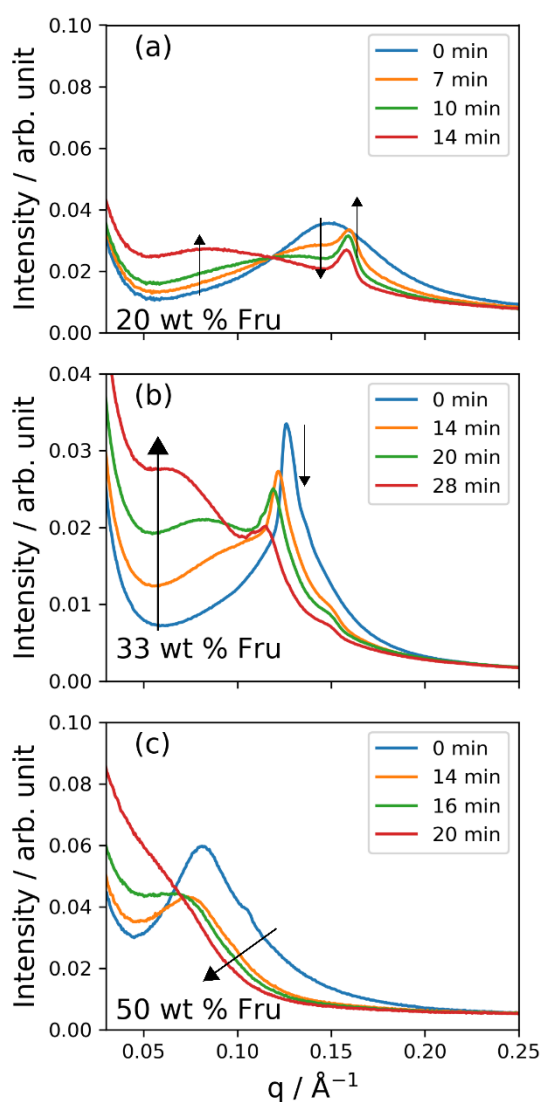
368 Figure 5. 1D SAXS patterns during ozonolysis of mixtures of: (a) 20 wt % fructose, (b) 33 wt
% fructose and (c) 50 wt % fructose. Note the shift to low-*q* of the broad inverse micellar peak
370 for each composition. An additional phase appears in the first few minutes of reaction for the
20 wt % fructose mixture (a). The additional peaks associated with the ordered inverse micellar
372 (P6₃/mmc) are revealed after ~ 20 min for the 33 wt % fructose mixture (b) – these are indexed
in the ESI. [O_3] = 77 ± 5 ppm, RH < 5 %. The black arrows indicate the progression of different
374 peaks from ordered phases with time as a visual guide.

We subjected proxy coatings of fatty acid-fructose mixtures to ozonolysis under dry conditions
376 analogous to our previous film kinetic study (Milsom et al., 2021a). Figure 5 presents the SAXS
patterns and phases observed during ozonolysis for the fructose-containing mixtures studied
378 here. There are broad peaks characteristic of the inverse micellar phase in all mixtures, this
was the most commonly observed phase under these conditions. An extra feature from an
380 ordered phase appears during ozonolysis for the 20 wt % fructose mixture (Fig. 5(a)) – this is
discussed in conjunction with simultaneous Raman spectrometry later (see Fig. 7). An ordered
382 phase is observed for the 33 wt % fructose film (Fig. 5(b)). Initially, the less intense peaks
associated with this phase are obscured by the broad overlapping inverse micellar peak. After
384 ~ 20 min of ozonolysis the broad peak has shifted to lower *q* and the other peaks are visible.
These peaks index closest to a hexagonal close-packed inverse micellar phase with P6₃/mmc
386 symmetry, which has been observed before in levitated droplets of a similar proxy (Pfrang et
al., 2017) – see ESI for phase indexing. This allowed us to measure the kinetic difference
388 between ordered and disordered inverse micellar phases.
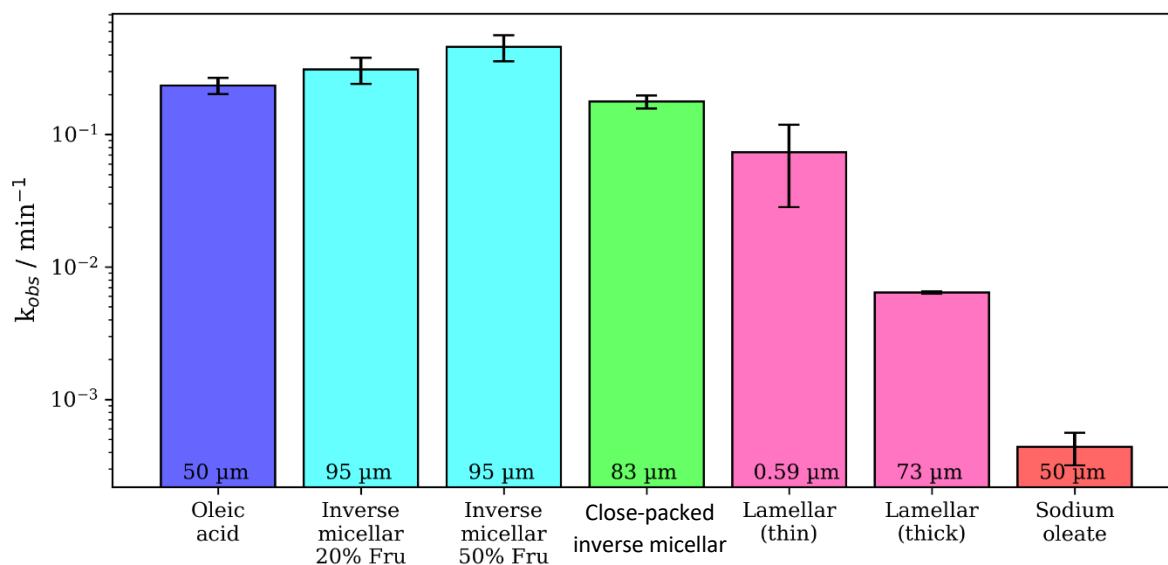
390

Figure 6. Pseudo-first order decay constants (k_{obs}) measured for the oleic acid-ozone reaction
392 carried out on coated films of different composition and nanostructure. The thickness of each
film is displayed at the bottom of each bar (see Table S1 in the ESI for all kinetic data and
394 associated uncertainties). Oleic acid, sodium oleate and lamellar phase data are taken from
earlier work (Milsom et al., 2021a). The lamellar phase was formed in a dry mixture of oleic
396 acid: sodium oleate (1:1 wt). Oleic acid and sodium oleate decays were measured by following
the C=C peak in the Raman spectrum as described in the methods. [O_3] = 77 ± 5 ppm and RH
398 < 5 %.

Reaction kinetics can be followed by SAXS using an analysis technique that we have
400 developed (Milsom et al., 2021a). We took advantage of the time resolution offered by a

synchrotron experiment to derive kinetic parameters for coated organic films of different
composition and nanostructure (Fig. 6). All kinetic data are summarised in Table S1 and a
more detailed derivation of these kinetic decay parameters is presented in Milsom et al.
(2021a).

The disordered inverse micellar phase reacts faster than the ordered micellar phase coated
at a similar thickness. This is to be expected as the close-packed inverse micelles are locked
into their position, increasing the viscosity of the phase and therefore slowing the diffusion of
small molecules such as ozone. The viscosity of close-packed inverse micelles can be in the
order of 10^4 times higher than for the disordered inverse micelles (Pouzot et al., 2007).

An order of reactivity exists between nanostructures. We are now able to compare the
reactivity of different phases formed by this proxy system and the reactivity of its constituent
parts (Fig. 6). Going from most to least reactive: inverse micellar > close-packed inverse
micellar > (dry) lamellar. Note that the lamellar phase in this case is anhydrous. As suggested
by Hearn *et al.*, diffusion of ozone past the closely packed lamellar chains is likely to be
hindered and the rate of reaction reduced as a result, limiting the reaction to the surface of the
film (Hearn et al., 2005).
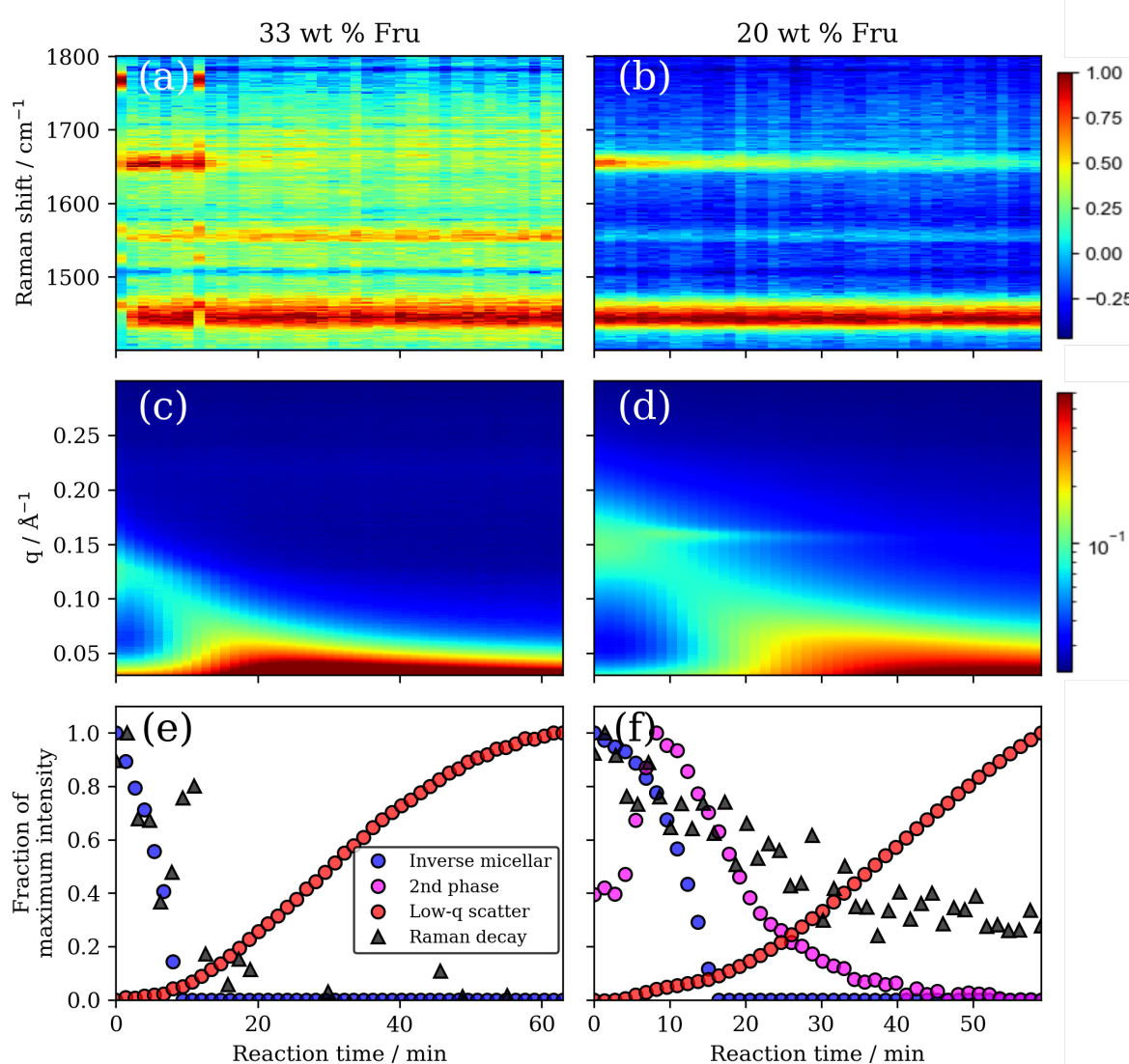
Figure 7. (a) and (b) Raman spectra vs reaction time highlighting the disappearance of the
oleic acid C=C peak at ~ 1650 cm^{-1} and the persistence of the –CH$_2$ deformation band at ~

420 1442 cm^{-1} for the 33 and 20 wt % fructose compositions, respectively. (c) and (d) simultaneous SAXS patterns vs reaction time showing the initial broad inverse micellar peak (0.12-0.15 Å^{-1})
422 which shifts to lower q and disappears. The increase in low-q scattering is also evident along with the appearance of a 2nd phase peak for the 20 wt % fructose composition (d). (e) and (f)
424 Plots of maximum peak area intensity vs reaction time for key SAXS and Raman peaks. Raman decay is measured by following the C=C/-CH$_2$ peak area ratio.

426 The close-packed (ordered) inverse micellar phase film was ~ 12 μm thinner than the inverse micellar films. We have shown previously that film thickness can affect reactivity (Milsom et
428 al., 2021a), so we cannot rule out the effect of film thickness in these experiments. Though it was not possible to control film thickness, comparisons are still possible and actually reveal
430 some stark differences in reactivity. Most notably is the comparison of the sub-micron lamellar phase film with ~ 95 μm films of inverse micellar phase. The thin lamellar phase film reacts
432 slower than the inverse micellar films despite the ~ 160-fold difference in film thicknesses. There is also a difference of nearly two orders of magnitude in reactivity between the thickest
434 lamellar film (73 μm) and the inverse micellar films (95 μm).

       The inverse micellar d-spacing increases (q decreases) as ozonolysis progresses (Fig. 7).
436 This experiment was carried out under dry conditions, so the increase in spacing must be a result of the reaction rather than any water uptake. We suggest that fructose itself reacts with
438 one of the intermediate products. Common saccharides found in the atmosphere, including glucose (closely related to fructose), have been shown to react readily with Criegee
440 intermediates that are formed as a result of ozonolysis (Enami et al., 2017). This forms ethers of greater mass and therefore products are likely to take up more space, accounting for the
442 increase in d-spacing observed during our ozonolysis experiment. Fructose can form an ether with oleic acid, however, to the author's knowledge, this has only been observed as an
444 enzymatic reaction (Ye and Hayes, 2011). Reaction with a Criegee intermediate is therefore the most probable explanation.

446 Products may themselves self-assemble. The increase in low-q scattering observed here was not observed during reactions of similar samples without fructose (Milsom et al., 2021a). This
448 suggests that the species causing the increased low-q scatter is associated with the fructose in the system. If high-molecular-weight fructose products are formed, the marked increase in
450 low-q scatter suggests that these molecules aggregate into structures with large repeat distances.

452 A new phase was formed with a peak in q-range of $ca.$ 0.14–0.16 Å during the ozonolysis of the 20 wt % fructose mixture (Fig. 5(a) and Fig. 7(d)). This was unexpected as it was assumed
454 that self-assembly would be destroyed by chemical reaction of the constituent fatty acid, as observed previously (Pfrang et al., 2017; Milsom et al., 2021a). This phase took longer to
456 disappear compared with the initial inverse micellar phase. The reaction induced heterogeneity in the film both in the nanostructure and corresponding physical properties. This
458 observation suggests that there is a dynamic relationship between nanostructure and the chemical reaction of this fatty acid aerosol proxy. The identity of this phase is uncertain due to
460 the lack of a 2nd order peak in the SAXS pattern, however this peak appears where the dry lamellar phase peak is expected to occur (Milsom et al., 2021a; Mele et al., 2018) – this is the
462 most likely arrangement. The atmospheric implications of the effect of nanostructure on reaction kinetics will be discussed in the following section.

464 There is evidence that the oleic acid double-bond persists at the end of the reaction (Fig. 7(b)). Simultaneous Raman spectroscopy on our deposited films shows clearly that the carbon-
466 carbon double-bond peak associated with oleic acid is still present at the end of the reaction even though the initial SAXS peaks are not visible. The increase in inverse micellar d-spacing

468   (SAXS peak shift to lower q), the notable increase in low-q scattering and the persistence of the double-bond suggests that oleic acid may be protected by the increase in viscosity

470   expected by the formation of larger molecular mass molecules, which have been identified as products for the oleic acid-ozone system (Reynolds et al., 2006; Zahardis et al., 2005). This

472   persistence is consistent with most of the recent work on coated capillaries and residues observed after oxidising monolayers of atmospheric surfactants (including oleic acid) coated

474   on water (Milsom et al., 2021a; Woden et al., 2021; Woden et al., 2018; Sebastiani et al., 2022; Sebastiani et al., 2018; Pfrang et al., 2014; for completeness, it should be noted that

476   King et al., 2009, also reported a residue following oleic acid ozonolysis, although this finding was subsequently reported to be likely caused by an impurity in the deuterated sample used

478   in this early study and there was no evidence of such a residue in their most recent work, see King et al., 2020). This highlights the utility of a simultaneous technique to measure reaction

480   kinetics (Raman spectroscopy).

482   **Atmospheric implications**

    A wide distribution of aerosol phase states in the atmosphere has been observed and

484   predicted with global chemistry models (Shiraiwa et al., 2017; Schmedding et al., 2020; Virtanen et al., 2010). This phase state is dependent on the aerosol's environment, which

486   includes humidity and temperature. Aerosol multiphase processes are strongly affected by the formation of semi-solid and glassy phases due to reduced gas-particle interactions and the

488   effect on particle diffusivity (Berkemeier et al., 2016; Zhou et al. 2019; Zhou et al. 2013; Mikhailov et al., 2009: Koop et al., 2011; Zobrist et al., 2011). This in turn leads to phase-

490   dependent increases in aerosol atmospheric lifetimes and can facilitate the long-range transport of an aerosol substantially. Particle phase state and viscous aerosol organic coatings

492   have been linked to the long-range transport of polycyclic aromatic hydrocarbons (PAHs), which are particularly harmful to human health by acting as carcinogens (Shrivastava et al.,

494   2017; Mu et al., 2018).

    In the work presented here, we are adding a further organic aerosol component to our bottom-

496   up approach for this fatty acid aerosol proxy system with the addition of the sugar fructose, which is commonly found in urban and marine emissions. The addition of fructose induces

498   nano-structural changes by acting as a kosmotrope under humidified conditions. This shows that the nanostructure depends on the organic composition in addition to the relative humidity.

500   The presence of other aerosol components will likely impact the self-assembly reported here, but, we expect that fatty acid self-assembly still occurs in their presence as briefly outlined

502   below (compare discussion in Pfrang et al., 2017). Uncharged water-soluble components have been shown to dissolve in the aqueous region of the self-assembled structure, acting as a

504   humectant (in addition to the role as kosmotrope demonstrated for fructose in the present work) and allowing the self-assembly to occur at lower humidities. Charged water-soluble

506   inorganic components will have the same effect, but in addition, by changing the ionic strength and head group charge, will shift the phase boundaries between different self-assembled

508   structures. Hydrophobic aerosol components will partition into the non-aqueous regions of the self-assembled phases promoting the formation of inverse ('water-in-oil') phases.

510   In this study, we quantify two key properties affected by the nanostructure: hygroscopicity and reactivity. As illustrated in Fig. 4, the nanostructure increases the hygroscopicity parameter (κ)

512   by as much as a factor of ca. 10 to 50 compared to liquid oleic acid. Hygroscopicity determines the water uptake of aerosol at a specific RH; we have previously shown (Milsom et al., 2022a)

514   that aerosol water content strongly impacts on viscosity. Fig. 6 shows that the aerosol reactivity changes by nearly two orders of magnitude when altering the nano-structural

516   arrangement e.g. between a 73-µm thick lamellar film and a 95-µm thick inverse micellar film. This strong effect on aerosol reactivity associated with the nanostructure is likely due to

518   changes in viscosity and diffusivity. We acknowledge that the film thicknesses given in Fig. 6 are comparatively thick considering that most atmospheric aerosols accumulate in the 0.1–

520   2.5-µm range. However, as discussed in Pfrang et al. (2017), for thermodynamically equilibrated phases, no substantial size dependence is expected and we could confirm

522   consistent self-assembly from 500-nm films to 2-mm droplets, i.e. covering the key size range for atmospheric particles. If some of the phases identified in our atmospheric aerosol proxy

524   were not thermodynamically stable states, the exact phase observed at a given point in the experiment would depend on timescales and therefore droplet size/film thickness, but complex

526   self-assembly would still be expected to occur. In Milsom et al. (2021) we have reported the film thickness-dependent kinetic behaviour and measured the effect of the organic phase on

528   the kinetics.

    Previously, we have shown that ozonolysis destroys self-assembly in fatty acid aerosol proxies

530   (Pfrang et al., 2017; Milsom et al., 2021a). Here we additionally show that ozonolysis can induce the formation of a new intermediate molecular arrangement (see Fig. 7(d)),

532   demonstrating the possibility that self-assembly could be induced by the chemical reaction of these atmospheric molecules with ozone. This, in combination with humidity-induced phase

534   changes, suggests a dynamic aerosol phase state which is dependent on the molecular arrangement of the surfactant molecules.

536   Atmospheric aerosols exhibit heterogeneity both in terms of composition and physical properties (Kirpes et al., 2019; Schill et al., 2015). Particle viscosity can become

538   heterogeneous during chemical reaction and exposure to humidity (Hosny et al., 2016). We have now demonstrated that nano-structural heterogeneity exists during humidity change and

540   ozonolysis where different nanostructures coexist. There must therefore be a heterogeneity in hygroscopicity in our proxy films due to the link between nanostructure and κ (see Fig. 4). The

542   formation of an intermediate nanostructure during ozonolysis observed here suggests that viscosity may not be equal throughout the film and that the diffusivity of small molecules such

544   as ozone throughout the particle would also not be uniform, affecting the lifetime of the proxy (Shiraiwa et al, 2011b). The increase in *d*-spacing we observed between inverse micelles

546   during ozonolysis suggests that larger molecules are formed as a result of the reaction (see Fig. 5 and Fig. 7(c) & (d)). These larger molecules may also contribute to film heterogeneity

548   and alter the reactive lifetime of these molecules.

    Sugars and fatty acids, such as fructose and oleic acid, are commonly encountered

550   components of aerosols emitted in urban (Wang et al., 2006) and marine (Fu et al., 2013) environments. Specifically, saccharides (sugars) have been identified along with fatty acids

552   as major components of thick (µm-scale) organic coatings observed on sea spray aerosols (Kirpes et al., 2019) and also in a cafeteria environment (Alves et al., 2020), demonstrating

554   the wide range of environments our proxies represent. Their relative abundances can vary significantly depending on season, time of day and location. In this study we have shown that

556   the proxy sugar content has a substantial impact on aerosol physical properties via a change in nanostructure. We conclude that, as the relative amount of sugar and fatty acid changes

558   between environments, nanostructures could also vary depending on the location and emission type.

560   We have now demonstrated that the reactivity of surface-active oleic acid depends not only on whether it is self-assembled (Pfrang et al., 2017; Milsom et al., 2021a), but also on the

562   specific nanostructure it adopts (see Fig. 7). Our results suggest that the lifetime of surfactant material would depend on nanostructure, which in turn is linked to aerosol composition and

564 which is also affected by relative humidity. We would expect complex behaviour associated with humidity changes given that nanostructure both influences and is influenced by humidity.

566 The associated surfactant lifetime will also change. It should be noted that we have carried out the ozonolysis experiments presented here only at low humidity and at high ozone levels;

568 the possible implications of this deviation from atmospheric conditions would merit further investigation (noting experimental challenges associated with interfering reactions of highly

570 reactive OH radicals potentially produced in ozonolysis studies at high humidities). Our earlier modelling work (Milsom et al., 2022b) estimated significantly extended half-lives of

572 nanostructured (lamellar-phase) oleic acid for a range of atmospherically relevant film thicknesses and ozone levels (e.g. a half-life increase of ca. 10 days for a 0.75 µm film in ca.

574 25 ppb ozone; see Fig. 7 in Milsom et al., 2022b). The persistence of surface-active material has been demonstrated experimentally at the air-water interface (Woden et al., 2021; Woden

576 et al., 2018; Sebastiani et al., 2022; Sebastiani et al., 2018; Pfrang et al., 2014). Simultaneous Raman microscopy suggests that oleic acid can persist in the films studied here, a finding

578 consistent with non-fructose-containing films of this proxy (Milsom et al., 2021a). We have demonstrated that the reactive lifetime of oleic acid can vary by orders of magnitude as a result

580 of different molecular arrangements. There is a link between surfactant content and cloud droplet formation potential as a result of a reduction in surface tension (Bzdek et al., 2020;

582 Ovadnevaite et al., 2017; Facchini et al., 2000; Facchini et al., 1999). Therefore, any increase in surfactant lifetime would imply a similar increase of the cloud formation potential of a

584 surfactant-containing aerosol, such as aerosols emitted from cooking or sea spray containing oleic acid and/or related species.

586

Conclusions

588 Our work has clearly shown that changes in the nanostructure, induced by humidity changes, can directly affect both water uptake and reactivity which are known to be two key aerosol

590 ageing processes.[e.g. Pöschl, 2005]

Crucially, we have demonstrated and quantified the direct link between the nanostructures

592 formed by fructose-containing fatty acid mixtures and the key aerosol properties of hygroscopicity and reactivity for the first time by utilising synchrotron SAXS and complimentary

594 Raman microscopy. This combination of SAXS and Raman data allowed us to infer key atmospheric aerosol properties and extract information from coexistent nanostructures to draw

596 comparisons between these. As a result, heterogeneity could be revealed during humidity exposure and ozonolysis. Our findings demonstrate that self-assembly of fatty acid

598 nanostructures can alter both water uptake and chemical reactivity. We have also shown that ozonolysis can induce the formation of a new intermediate molecular arrangement,

600 demonstrating the possibility that self-assembly could be induced by the chemical reaction of these atmospheric components with ozone. This, in combination with humidity-induced phase

602 changes, suggests a dynamic aerosol phase state which is dependent on the molecular arrangement of the surfactant molecules.

604 Our work demonstrated the fundamental effects of nanostructure on water uptake and reactivity. While these parameters in turn affect the particles´ impacts on air quality and

606 climate, a direct assessment of these effects is not within the scope of the work presented here.

608

Data access statement

610 Data supporting with this study are available in the supporting information and from the corresponding author upon request.

612

Conflicts of interest

614 There are no conflicts to declare.

616 **Acknowledgements**

This work was carried out with the support of the Diamond Light Source (DLS), instrument I22
618 (proposal SM21663). AM wishes to acknowledge funding from NERC SCENARIO DTP award number NE/L002566/1 and CENTA DTP. The work was supported by NERC (research grant
620 NE/T00732X/1). The authors would like to thank Nick Terrill (DLS), Tim Snow (DLS) and Lee Davidson (DLS) for technical support during beamtime experiments; Jacob Boswell is
622 acknowledged for help at beamtimes. The authors are grateful to the Central Laser Facility for access to key equipment for the Raman work simultaneously to the DLS beamtime
624 experiments.

626 **References**

Alpert, P. A., P. C. Arroyo, J. Dou, U. K. Krieger, S. S. Steimer, J.-D. Förster, F. Ditas, C.
628   Pöhlker, S. Rossignol, M. Passananti, S. Perrier, C. George, M. Shiraiwa, T. Berkemeier, B. Watts and M. Ammann, *Phys. Chem. Chem. Phys.*, 2019, **21**, 20613–
630   20627

Alves, C. A., E. D. Vicente, M. Evtyugina, A. M. Vicente, T. Nunes, F. Lucarelli, G. Calzolai,
632   S. Nava, A. I. Calvo, C. del B. Alegre, F. Oduber, A. Castro and R. Fraile, *Atmos. Pollut. Res.*, 2020, **11**, 531–544.

634 Asghar, K. A., D. A. Rowlands, J. M. Elliott and A. M. Squires, *ACS Nano*, 2015, **9**, 10970–10978.

636 Bahadur, J., A. Das and D. Sen, *J. Appl. Crystallogr.*, 2019, **52**, 1169–1175.

Berkemeier, T., S. S. Steimer, U. K. Krieger, T. Peter, U. Pöschl, M. Ammann and M.
638   Shiraiwa, *Phys. Chem. Chem. Phys.*, 2016, **18**, 12662–12674.

Boucher, O., D. Randall, P. Artaxo, C. Bretherton, G. Feingold, P. Forster, V.-M. Kerminen,
640   Y. Kondo, H. Liao, U. Lohmann, P. Rasch, S. K. Satheesh, S. Sherwood, B. Stevens and X. Y. Zhang, in *Climate Change 2013 - The Physical Science Basis*, ed.
642   Intergovernmental Panel on Climate Change, Cambridge University Press, Cambridge, 2013, pp. 571–658.

644 Bzdek, B. R., J. P. Reid, J. Malila and N. L. Prisle, *Proc. Natl. Acad. Sci. U. S. A.*, 2020, **117**, 8335–8343.

646 Chan, C. K. and X. Yao, *Atmos. Environ.*, 2008, **42**, 1–42.

Chen, Z. and R. P. Rand, *Biophys. J.*, 1997, **73**, 267–276.

648 Clegg, S. L., P. Brimblecombe and A. S. Wexler, *J. Phys. Chem. A*, 1998, **102**, 2155–2171.

Enami, S., M. R. Hoffmann and A. J. Colussi, *J. Phys. Chem. Lett.*, 2017, **8**, 3888–3894.

650 Facchini, M. C., S. Decesari, M. Mircea, S. Fuzzi and G. Loglio, *Atmos. Environ.*, 2000, **34**,

4853–4857.

652   Facchini, M. C., M. Mircea, S. Fuzzi and R. J. Charlson, *Nature*, 1999, **401**, 257–259.

Fredenslund, A., R. L. Jones and J. M. Prausnitz, *AIChE J.*, 1975, **21**, 1086–1099.

654   Fu, P. Q., K. Kawamura, J. Chen, B. Charrière and R. Sempéré, *Biogeosciences*, 2013, **10**, 653–667.

656   Fu, P., K. Kawamura, K. Okuzawa, S. G. Aggarwal, G. Wang, Y. Kanaya and Z. Wang, *J. Geophys. Res. Atmos.*, 2008, **113**, 1–20.

658   Gallimore, P. J., P. T. Griffiths, F. D. Pope, J. P. Reid and M. Kalberer, *J. Geophys. Res.*, 2017, **122**, 4364–4377.

660   Harrison, R. M. *Philos. Trans. R. Soc. A Math. Phys. Eng. Sci.*, 2020, **378**, 20190319.

Hearn, J. D., G. D. Smith and A. J. Lovett, *Phys. Chem. Chem. Phys.*, 2005, **7**, 501–511.

662   Hosny, N. A., C. Fitzgerald, A. Vyšniauskas, A. Athanasiadis, T. Berkemeier, N. Uygur, U. Pöschl, M. Shiraiwa, M. Kalberer, F. D. Pope and M. K. Kuimova, *Chem. Sci.*, 2016,
664   **7**, 1357–1367.

Iwahashi, M., Y. Yamaguchi, T. Kato, T. Horiuchi, I. Sakurai and M. Suzuki, *J. Phys. Chem.*,
666   1991, **95**, 445–451.

Jimenez, J. L., M. R. Canagaratna, N. M. Donahue, A. S. H. Prevot, Q. Zhang, J. H. Kroll, P.
668   F. DeCarlo, J. D. Allan, H. Coe, N. L. Ng, A. C. Aiken, K. S. Docherty, I. M. Ulbrich, A.
        P. Grieshop, A. L. Robinson, J. Duplissy, J. D. Smith, K. R. Wilson, V. A. Lanz, C.
670   Hueglin, Y. L. Sun, J. Tian, A. Laaksonen, T. Raatikainen, J. Rautiainen, P.
        Vaattovaara, M. Ehn, M. Kulmala, J. M. Tomlinson, D. R. Collins, M. J. Cubison, J.
672   Dunlea, J. A. Huffman, T. B. Onasch, M. R. Alfarra, P. I. Williams, K. Bower, Y.
        Kondo, J. Schneider, F. Drewnick, S. Borrmann, S. Weimer, K. Demerjian, D.
674   Salcedo, L. Cottrell, R. Griffin, A. Takami, T. Miyoshi, S. Hatakeyama, A. Shimono, J.
        Y. Sun, Y. M. Zhang, K. Dzepina, J. R. Kimmel, D. Sueper, J. T. Jayne, S. C.
676   Herndon, A. M. Trimborn, L. R. Williams, E. C. Wood, A. M. Middlebrook, C. E. Kolb,
        U. Baltensperger and D. R. Worsnop, *Science (80-.).*, 2009, **326**, 1525–1529.

678   Kang, M., F. Yang, H. Ren, W. Zhao, Y. Zhao, L. Li, Y. Yan, Y. Zhang, S. Lai, Y. Zhang, Y.
        Yang, Z. Wang, Y. Sun and P. Fu, *Sci. Total Environ.*, 2017, **607**–**608**, 339–350.

680   King, M. D., S. H. Jones, C. O. M. Lucas, K. C. Thompson, A. R. Rennie, A. D. Ward, A. A.
        Marks, F. N. Fisher, C. Pfrang, A. V. Hughes and R. A. Campbell, *Phys. Chem.*
682   *Chem. Phys.*, 2020, **22**, 28032.

King, M. D., A. R. Rennie, C. Pfrang, A. V. Hughes and K. C. Thompson, *Atmos. Environ.*,
684   2010, **44**, 1822–1825.

King, M. D., A. R. Rennie, K. C. Thompson, F. N. Fisher, C. C. Dong, R. K. Thomas, C.
686   Pfrang and A. V. Hughes, *Phys. Chem. Chem. Phys.*, 2009, **11**, 7699–7707.

Kirpes, R. M., D. Bonanno, N. W. May, M. Fraund, A. J. Barget, R. C. Moffet, A. P. Ault and
688   K. A. Pratt, *ACS Cent. Sci.*, 2019, **5**, 1760–1767.

Koop, T., J. Bookhold, M. Shiraiwa and U. Pöschl, *Phys. Chem. Chem. Phys.*, 2011, **13**,
690   19238–19255.

Koynova, R., J. Brankov and B. Tenchov, *Eur. Biophys. J.*, 1997, **25**, 261–274.

692   Kulkarni, C. V., W. Wachter, G. Iglesias-Salto, S. Engelskirchen and S. Ahualli, *Phys. Chem.*
        Chem. Phys., 2011, **13**, 3004–3021.

694 Li, G., H. Su, N. Ma, J. Tao, Y. Kuang, Q. Wang, J. Hong, Y. Zhang, U. Kuhn, S. Zhang, X. Pan, N. Lu, M. Tang, G. Zheng, Z. Wang, Y. Gao, P. Cheng, W. Xu, G. Zhou, C.

696 Zhao, B. Yuan, M. Shao, A. Ding, Q. Zhang, P. Fu, Y. Sun, U. Pöschl and Y. Cheng, *Faraday Discuss.*, 2021, DOI:10.1039/D0FD00099J.

698 Li, T., A. J. Senesi and B. Lee, *Chem. Rev.*, 2016, **116**, 11128–11180.

Libster, D., P. Ben Ishai, A. Aserin, G. Shoham and N. Garti, *Langmuir*, 2008, **24**, 2118–

700 2127.

Lindblom, G. and G. Orädd, *Prog. Nucl. Magn. Reson. Spectrosc.*, 1994, **26**, 483–515.

702 Liu, J., F. Zhang, W. Xu, L. Chen, J. Ren, S. Jiang, Y. Sun and Z. Li, *J. Geophys. Res. Atmos.*, 2021, **126**, 1–11.

704 Mele, S., O. Söderman, H. Ljusberg-Wahrén, K. Thuresson, M. Monduzzi and T. Nylander, *Chem. Phys. Lipids*, 2018, **211**, 30–36.

706 Mikhailov, E., S. Vlasenko, S. T. Martin, T. Koop and U. Pöschl, *Atmos. Chem. Phys.*, 2009, **9**, 9491–9522.

708 Milsom, A., A. M. Squires, A. D. Ward and C. Pfrang, *Acc. Chem. Res.*, 2023, **56**, 2555–2568.

710 Milsom, A., A. M. Squires, I. Quant, N. J. Terrill, S. Huband, B. Woden, E. R. Cabrera-Martinez and C. Pfrang, *J. Phys. Chem. A*, 2022a, **126**, 7331–7341.

712 Milsom, A., A. M. Squires, A. D. Ward and C. Pfrang, *Atmos. Chem. Phys.*, 2022b, **22**, 4895–4907.

714 Milsom, A., A. M. Squires, M. W. A. Skoda, P. Gutfreund, E. Mason, N. J. Terrill and C. Pfrang, *Environ. Sci. Atmos.*, 2022c, **2**, 964–977.

716 Milsom, A., A. M. Squires, B. Woden, N. J. Terrill, A. D. Ward and C. Pfrang, *Faraday Discuss.*, 2021a, **226**, 364–381.

718 Milsom, A., A. M. Squires, J. A. Boswell, N. J. Terrill, A. D. Ward and C. Pfrang, *Atmos. Chem. Phys.*, 2021b, **21**, 15003–15021, doi.org/10.5194/acp-21-15003-2021.

720 Mu, Q., M. Shiraiwa, M. Octaviani, N. Ma, A. Ding, H. Su, G. Lammel, U. Pöschl and Y. Cheng, *Sci. Adv.*, 2018, **4**, eaap7314.

722 Orädd, G., G. Lindblom, K. Fontell and H. Ljusberg-Wahren, *Biophys. J.*, 1995, **68**, 1856–1863.

724 Ots, R., M. Vieno, J. D. Allan, S. Reis, E. Nemitz, D. E. Young, H. Coe, C. Di Marco, A. Detournay, I. A. Mackenzie, D. C. Green and M. R. Heal, *Atmos. Chem. Phys.*, 2016,

726 **16**, 13773–13789.

Ovadnevaite, J., A. Zuend, A. Laaksonen, K. J. Sanchez, G. Roberts, D. Ceburnis, S.

728 Decesari, M. Rinaldi, N. Hodas, M. C. Facchini, J. H. Seinfeld and C. O'Dowd, *Nature*, 2017, **546**, 637–641.

730 Parsegian, V. A., N. Fuller and R. P. Rand, *Proc. Natl. Acad. Sci. U. S. A.*, 1979, **76**, 2750–2754.

732 Pauw, B. R. *J. Phys. Condens. Matter*, 2013, **25**, 383201.

Petters, M. D. and S. M. Kreidenweis, *Atmos. Chem. Phys.*, 2007, **7**, 1961–1971.

734 Pfrang, C., K. Rastogi, E. R. Cabrera-Martinez, A. M. Seddon, C. Dicko, A. Labrador, T. S. Plivelic, N. Cowieson and A. M. Squires, *Nat. Commun.*, 2017, **8**, 1724.

736   Pfrang, C., F. Sebastiani, C. O. M. Lucas, M. D. King, I. D. Hoare, D. Chang and R. A. Campbell, *Phys. Chem. Chem. Phys.*, 2014, **16**, 13220–13228.

738   Pfrang, C., M. Shiraiwa and U. Pöschl, *Atmos. Chem. Phys.*, 2011, **11**, 7343–7354.

Pfrang, C., M. Shiraiwa and U. Pöschl, *Atmos. Chem. Phys.*, 2010, **10**, 4537–4557.

740   Pöschl, U. *Angew. Chemie Int. Ed.*, 2005, **44**, 7520–7540.

Pouzot, M., R. Mezzenga, M. Leser, L. Sagalowicz, S. Guillote and O. Glatter, *Langmuir*,
742   2007, **23**, 9618–9628.

Reid, J. P., A. K. Bertram, D. O. Topping, A. Laskin, S. T. Martin, M. D. Petters, F. D. Pope
744   and G. Rovelli, *Nat. Commun.*, 2018, **9**, 1–14.

Renbaum-Wolff, L., J. W. Grayson, A. P. Bateman, M. Kuwata, M. Sellier, B. J. Murray, J. E.
746   Shilling, S. T. Martin and A. K. Bertram, *Proc. Natl. Acad. Sci.*, 2013, **110**, 8014–8019.

Reynolds, J. C., D. J. Last, M. McGillen, A. Nijs, A. B. Horn, C. Percival, L. J. Carpenter and
748   A. C. Lewis, *Environ. Sci. Technol.*, 2006, **40**, 6674–6681.

Richardson, S. J., P. A. Staniec, G. E. Newby, J. L. Rawle, A. R. Slaughter, N. J. Terrill, J.
750   M. Elliott and A. M. Squires, *Chem. Commun.*, 2015, **51**, 11386–11389.

Rickards, A. M. J., R. E. H. Miles, J. F. Davies, F. H. Marshall and J. P. Reid, *J. Phys. Chem.*
752   *A*, 2013, **117**, 14120–14131.

Rudich, Y., N. M. Donahue and T. F. Mentel, *Annu. Rev. Phys. Chem.*, 2007, **58**, 321–352.

754   Schill, S. R., D. B. Collins, C. Lee, H. S. Morris, G. A. Novak, K. A. Prather, P. K. Quinn, C.
M. Sultana, A. V. Tivanski, K. Zimmermann, C. D. Cappa and T. H. Bertram, *ACS*
756   *Cent. Sci.*, 2015, **1**, 132–141.

Schmedding, R., Q. Z. Rasool, Y. Zhang, H. O. T. Pye, H. Zhang, Y. Chen, J. D. Surratt, F.
758   D. Lopez-Hilfiker, J. A. Thornton, A. H. Goldstein and W. Vizuete, *Atmos. Chem.*
Phys., 2020, **20**, 8201–8225.

760   Sebastiani, F., R. A. Campbell and C. Pfrang, *Environ. Sci.: Atmos.*, 2022, **2**, 1324–1337.

Sebastiani, F., R. A. Campbell, K. Rastogi and C. Pfrang, *Atmos. Chem. Phys.*, 2018, **18**,
762   3249–3268.

Seddon, J. M., E. A. Bartle and J. Mingins, *J. Phys. Condens. Matter*, 1990, **2**, SA285–
764   SA290.

Shearman, G. C., A. I. I. Tyler, N. J. Brooks, R. H. Templer, O. Ces, R. V. Law and J. M.
766   Seddon, *Liq. Cryst.*, 2010, **37**, 679–694.

Shiraiwa, M., Y. Li, A. P. Tsimpidi, V. A. Karydis, T. Berkemeier, S. N. Pandis, J. Lelieveld,
768   T. Koop and U. Pöschl, *Nat. Commun.*, 2017, **8**, 1–7.

Shiraiwa, M., C. Pfrang, T. Koop and U. Pöschl, *Atmos. Chem. Phys.*, 2012, **12**, 2777–2794.

770   Shiraiwa, M., M. Ammann, T. Koop and U. Poschl, *Proc. Natl. Acad. Sci. U. S. A.*, 2011a,
108, 11003–11008.

772   Shiraiwa, M., M. Ammann, T. Koop and U. Pöschl, *Proc. Natl. Acad. Sci. USA*, 2011b, **108**,
11003-11008, Supplementary material: DOI:10.1073/pnas.1103045108/-
774   /DCSupplemental.

Shiraiwa, M., C. Pfrang and U. Pöschl, *Atmos. Chem. Phys.*, 2010, **10**, 3673–3691.

776   Shrivastava, M., C. D. Cappa, J. Fan, A. H. Goldstein, A. B. Guenther, J. L. Jimenez, C.

778 Kuang, A. Laskin, S. T. Martin, N. L. Ng, T. Petaja, J. R. Pierce, P. J. Rasch, P. Roldin, J. H. Seinfeld, J. Shilling, J. N. Smith, J. A. Thornton, R. Volkamer, J. Wang, D. R. Worsnop, R. A. Zaveri, A. Zelenyuk and Q. Zhang, *Rev. Geophys.*, 2017a, **55**, 780 509–559.

Shrivastava, M., S. Lou, A. Zelenyuk, R. C. Easter, R. A. Corley, B. D. Thrall, P. J. Rasch, J. 782 D. Fast, S. L. M. Simonich, H. Shen and S. Tao, *Proc. Natl. Acad. Sci. U. S. A.*, 2017b, **114**, 1246–1251.

784 Stavroulas, I., A. Bougiatioti, G. Grivas, E. Liakakou, K. Petrinoli, K. Kourtidis, E. Gerasopoulos and N. Mihalopoulos, *Sci. Total Environ.*, 2023, 786 DOI:10.1016/j.scitotenv.2023.168031.

Tandon, P., S. Raudenkolb, R. H. H. Neubert, W. Rettig and S. Wartewig, *Chem. Phys. 788 Lipids*, 2001, **109**, 37–45.

Tiddy, G. J. T., *Phys. Rep.*, 1980, **57**, 1–46.

790 Topping, D. O., G. B. McFiggans and H. Coe, *Atmos. Chem. Phys.*, 2005, **5**, 1205–1222.

Vicente, E. D., A. Vicente, M. Evtyugina, R. Carvalho, L. A. C. Tarelho, F. I. Oduber and C. 792 Alves, *Fuel Process. Technol.*, 2018, **176**, 296–306.

Virtanen, A., J. Joutsensaari, T. Koop, J. Kannosto, P. Yli-Pirilä, J. Leskinen, J. M. Mäkelä, J. 794 K. Holopainen, U. Pöschl, M. Kulmala, D. R. Worsnop and A. Laaksonen, *Nature*, 2010, **467**, 824–827.

796 Wang, Q. and J. Z. Yu, *Geophys. Res. Lett.*, 2021, DOI:10.1029/2021GL095130.

Wang, G., K. Kawamura, L. Shuncheng, K. Ho and J. Cao, *Environ. Sci. Technol.*, 2006, **40**, 798 4619–4625.

Wexler, A. S. and S. L. Clegg, *J. Geophys. Res.*, 2002, **107**, 4207.

800 Woden, B., M. W. A. Skoda, A. Milsom, C. Gubb, A. Maestro, J. Tellam and C. Pfrang, *Atmos. Chem. Phys.*, 2021, **21**, 1325–1340.

802 Woden, B., M. Skoda, M. Hagreen and C. Pfrang, *Atmosphere (Basel)*, 2018, **9**, 471.

Ye, R. and D. G. Hayes, *JAOCS, J. Am. Oil Chem. Soc.*, 2011, **88**, 1351–1359.

804 Zahardis, J. and G. A. Petrucci, *Atmos. Chem. Phys.*, 2007, **7**, 1237–1274.

Zahardis, J., B. W. LaFranchi and G. A. Petrucci, *J. Geophys. Res. D Atmos.*, 2005, **110**, 1– 806 10.

Zeng, J., Z. Yu, M. Mekic, J. Liu, S. Li, G. Loisel, W. Gao, A. Gandolfo, Z. Zhou, X. Wang, H. 808 Herrmann, S. Gligorovski and X. Li, *Environ. Sci. Technol. Lett.*, 2020, **7**, 76–81.

Zhao, Y., H. Huang, Y. Zhang, K. Wu, F. Zeng, J. Wang, X. Yu, Z. Zhu, X.-Y. Yu and F. 810 Wang, *Atmos. Environ.*, 2020, **220**, 117090.

Zhou, S., B. C. H. Hwang, P. S. J. Lakey, A. Zuend, J. P. D. Abbatt and M. Shiraiwa, *Proc. 812 Natl. Acad. Sci. U. S. A.*, 2019, **116**, 11658–11663.

Zhou, S., M. Shiraiwa, R. D. McWhinney, U. Pöschl and J. P. D. Abbatt, *Faraday Discuss.*, 814 2013, **165**, 391–406.

Zobrist, B., V. Soonsin, B. P. Luo, U. K. Krieger, C. Marcolli, T. Peter and T. Koop, *Phys. 816 Chem. Chem. Phys.*, 2011, **13**, 3514–3526.

Zuend, A., C. Marcolli, A. M. Booth, D. M. Lienhard, V. Soonsin, U. K. Krieger, D. O.

818   Topping, G. McFiggans, T. Peter and J. H. Seinfeld, *Atmos. Chem. Phys.*, 2011, **11**, 9155–9206.

820   Zuend, A., C. Marcolli, B. P. Luo and T. Peter, *Atmos. Chem. Phys.*, 2008, **8**, 4559–4593.